Facile synthesis of fullerene-C60 and rGO-supported KCdCl3-based halide perovskite nanocomposites toward effective electrode material for supercapacitor

Muhammad Riaz, Tauseef Munawar, Muhammad Shahid Nadeem, Faisal Mukhtar, Syed Danish Ali, Sumaira Manzoor, Muhammad Naeem Ashiq & Faisal Iqbal

Abstract

The family of halide perovskite materials is extremely large and has gained huge attention because of their low manufacturing cost and extraordinary structural, optical, electrical, and optoelectronic properties. These materials also deliver a pattern for designing new materials for energy conversion and energy storage applications. Here, we synthesized potassium cadmium chloride KCdCl3-based halide perovskite nanocomposites with rGO and fullerene-C60 by facile solvothermal method and studied their physical and electrochemical properties. The orthorhombic phase of KCdCl3 was confirmed from XRD spectra, and the existence of constituent elements (K, Cd, Cl, and C) was confirmed from EDX analysis. SEM images evident the successful anchoring of KCdCl3 particles over rGO and C60. BET results revealed the high surface area, pore radius, and pore volume of the KCdCl3/C60 electrodes. Furthermore, the electrochemical measurements demonstrated that KCdCl3/C60-based electrodes have a higher specific capacitance of 1135 F/g at 5 mV/s and cyclic stability (97.6% retention over 3000th cycles) than other grown electrodes. Also, GCD measurement results revealed that KCdCl3/C60 electrode has a high specific capacitance of 1420 F/g, an energy density of 2052 Wh/kg, and a power density of 4.19 W/kg at 1.0 A/g than other electrodes. Finally, intensive discussion proposed that halide perovskite nanocomposite electrodes can be used efficiently as supercapacitors electrode materials for future development in this field.

1 Introduction

Recently with the increasing intensive and avid demand for power and energy in industries, the rapid depletion of fossil fuels is creating a big energy crisis [1,2,3]. Therefore, the

fabrication of sustainable and proficient energy storage devices is necessary [4, 5]. Hence, the supercapacitor has gained much researcher interest as an emerging storage device. In light of the charge storage mechanism or cell configuration, the supercapacitor has two main classes, Pseudocapacitor and electric double-layer capacitor (EDLC) [6]. In Pseudocapacitor, a redox reaction takes place, and charges store faradically.
In contrast, in EDLC, no redox reaction occurs, although it contains a high specific surface area and store charge electrostatically (non-faradically) by the adsorption of electrolytic ions on the electrode materials [7]. Furthermore, in EDLC, no charge transfer occurs between electrolyte and electrode, and it has low energy density and specific capacitance compared to Pseudocapacitor [8]. As compared to other energy storage devices, the supercapacitor has many advantages, such as safety, superior cyclic stability, large power density, rapid charging-discharging rate, high reversibility, and outstanding power performance, making them promising candidates for next-generation energy storage devices [9,10,11].
Metal halide perovskites belong to the wonder and exciting class of nanomaterials for energy storage applications and have gained incredible research interest in the scientific community due to their remarkable optical, electronic, and ionic properties [12]. The generic formula for perovskites is ABX3, where A and B are monovalent and divalent cations, respectively, such as (A = CH3NH3^{+}(MA), CH(NH2)2^{+}(FA), Cs^{+}, Rb^{+}, K^{+}, B = Pb^{2+}, Sn^{2+}, Cd^{2+}, Cu^{2+}, and (X = I^{-}, Br^{-}, Cl^{-}, F^{-}) [13,14,15]. Inorganic perovskite materials are more stable in moisture and at high temperatures than organic halide perovskite. Kumar et al. reported that the metal halide perovskite CH3NH3PbBr3 single crystal has an energy density of 12.75 Wh/kg and volumetric capacitance of 429.1 F/cm^{3} at 5 mV/s, whereas low charge transfer resistance 4.4 k ohm/cm^{2} also exhibits remarkable cyclic stability [12]. Slonopas et al. reported that CH3NH3PbI3-based supercapacitors synthesized in a spark plasma sintering chamber exhibited a high energy density (34.2 Wh/kg) at 100 Hz [16]. In addition, Maji and his co-workers reported that CsPbI3 material showed a specific capacitance of 7.23 mF/cm^{2} at 2 mV/s and good cyclic stability [17].
Despite the improvement in the properties of halide perovskite materials used in energy storage applications, there are still certain challenges, including efficiency, scalability, and stability, which need to be addressed. Carbon-based materials, including metal-organic framework, carbon nanotubes, graphitic carbon nitride, fullerene, graphene oxide, and reduced graphene oxide, have played a positive and undeniable role in developing supercapacitor electrodes [18,19,20]. Reduced graphene oxide (rGO) is an exceptional candidate and has shown accelerated performance when incorporated with other nanocomposites because of its outstanding properties, such as good chemical and mechanical strength and high electrical and thermal conductivity [21]. Fullerene C60 has tremendous potential for energy storage applications due to its precise structure, high solubility, superb electron-accepting capacity, and extended redox chemistry [22]. Numerous efforts have been devoted to developing carbon-based nanocomposites as supercapacitor electrodes with enhanced performance [23]. Halide perovskites with carbon materials have improved the crystallinity and morphology of grown nanocomposite. Keeping in view, halide perovskites (KCdCl3) with carbon-based materials like rGO and C60 due to their good carriers' mobility, cyclic stability, large surface area, and high availability of pores are grown to achieve high specific capacitance [24] and studied their physical and electrochemical properties. Different approaches are reported to manufacture supercapacitors materials, such as the hydrothermal method, thermal evaporation, co-precipitation, sol–gel method, and solvothermal route.

The present study synthesized KCdCl3 and rGO, C60-based nanocomposites via a solvothermal route. The physical and electrochemical properties were studied using XRD, SEM, EDX, BET, IV, CV, GCD, EIS, ECSA, and LSV. The electrochemical measurements exhibit that rGO and C60-based electrodes have a higher storage ability.

2 Experimental

2.1 Materials

Potassium chloride (KCl), cadmium chloride (CdCl2), fullerene-C60 (purity 99.99%), Dimethylsulfoxide (DMSO), hydrochloric acid (HCL), and toluene were used as precursors. All the precursors were purchased from commercial source Sigma Aldrich and used as received without further process modification. Deionized water was used throughout the experiment.

2.2 Synthesis of KCdCl3 nanoparticles

A solvothermal approach was used for the synthesis of KCdCl3 nanoparticles. At the start of the experiment, 0.1 M of KCl and CdCl2 precursor with a 1:1 molar ratio was dissolved in 50 ml of DMSO and then stirred for 30 min at room temperature to prepare the homogenous solution. Afterward, 5 µL of HCl was added dropwise to the above suspension to avoid precipitation formation and ultrasonicated for 30 min to form a clear solution. Next, the solution was put in a Teflon-line autoclave for 7 h at 110 °C. Finally, cool down the autoclave and wash with deionized water, filter the settled material, dry at 120 °C for 2 h, and anneal at 300 °C for 2 h to get a fine powder.

2.3 Synthesis of KCdCl3/rGO and KCdCl3/C60 nanocomposite

First, as reported in the literature, rGO was chemically synthesized using Hummer's method [25, 26]. An appropriate amount of 3 g of graphite flake and 3 g of NaNO3 was added to a beaker and concentrated H2SO4 (150 cm^3) to form black-colored suspensions. To avoid exothermic reaction, the above suspension was kept in an ice bath, added 18 g of KMnO4 slowly and then stirred further for 1 h. Later, the ice bath was removed, and the suspension was further stirred for 48 h so that a brown slurry formed. The 500 mL of deionized water was added with H2O2 (1 wt%/500 cm^3). After this, washed with deionized water to separate the residue and solid product and dried under a vacuum for 6 h at 50 °C. Finally, GO was chemically reduced to rGO using hydrazine hydrate.
To synthesize KCdCl3/rGO nanocomposite, the weighted amount of the as-synthesized KCdCl3 particles and rGO (1:1) was added in 50 ml deionized water and ultrasonicate for 1 h and dried at 80 °C for 1 h. To synthesize KCdCl3/C60 nanocomposite, 1 g of pure C60 (purity 99.99%) was added to 50 ml toluene, followed by ultrasonication. Afterward, 20 ml of deionized water was added to evaporate toluene completely until the water phase became yellow. After this, 1 g of the as-synthesized KCdCl3 particles was added to the above suspension and further ultrasonicated for 2 h and finally dried at 80 °C for 2 h.

2.4 Electrochemical test

The electrochemical evaluation of the fabricated electrode was carried out in a three-electrode setup (Metrohm Autolab instrument PGSTAT-204) using 1 M KOH solution at ambient temperature, and various tests, including CV, GCD, EIS, LSV, and ECSA, were implemented. First, to obtain a homogenous slurry, the prepared sample (0.004 g) was thoroughly ground well into a fine powder, and Nafion binder was added in an amount so that slurry formed. After this, the slurry was coated on Ni-foam to make a working electrode. Then, to remove the impurities, the coated electrodes were dried in a Vacuum oven at ~ 80 °C overnight. The slurry was injected over Ni-foam. The CV measurement was achieved with a potential window − 0.05 to 0.5 V at different scan rates (5, 10, 15, 20, 25, 30 mV/s), and the GCD test was conducted within a potential window − 1.2 to 0.5 V at a constant 1 A/g current density. Furthermore, EIS calculations were performed in the frequency range 1×10^5 to 0.1 Hz keeping an AC voltage of 0.5 V. Also, LSV was recorded in the range of 0.0 to 0.5 V, while ECSA was conducted in the potential range of − 2.5 to 0.5 V.

2.5 Characterization

The structural and phase evaluation of the synthesized materials has been performed using an X-ray diffractometer (XRD) (Bruker-D8, Cu-Kα, λ = 1.54 Å, 2 θ = 10°–70°, 1.5 /min scanning rate; 40 kV/35 mA). The surface area, pore volume, and width were determined using Brunauer Emmett Teller (BET) analysis (specification listed in supporting information). Current–Voltage (IV) measurements were performed in the voltage range of − 10 to 10 V using a Keithley picometer (6487), two-probe setup. For IV measurements, the pellets of synthesized material were made and fabricated contacts with the silver paste by copper wire. The morphology and elemental content were studied by scanning electron microscope (Nova Nano SEM) equipped with EDX. The electrochemical studies (CV, GCD, EIS, LSV, and ECSA) were performed by the Metrohm Autolab instrument (PGSTAT- 204).

3 Results and discussion

3.1 X-ray diffraction (XRD) analysis

The X-ray diffraction (XRD) analysis is used to provide a detailed understanding of the phase purity and crystallinity of the synthesized material. The XRD profile of the synthesized products (KCdCl3, KCdCl3/rGO, and KCdCl3/C60) is shown in Fig. 1, along with the labeled diffraction planes. The observed diffraction peaks in all synthesized samples follow the standard data JCPDS # 00-018-0995 card, which confirmed that the orthorhombic phase KCdCl3 was successfully obtained and its composites with rGO and C60. A few additional peaks in the KCdCl3/C60 nanocomposite corresponding to JCPDS # 01-079-1715 of fullerene-C60 are further evidence of the formation of the KCdCl3/C60 composite. Additionally, the structural parameters such as lattice constants (a, b, c), the crystallite size (D), the volume of the unit cell (V), d-spacing, lattice strain (ε), and dislocation density (δ) were calculated by using the equation from the literature [27]. The calculated values are listed in Table 1. It is observed that a small alternation in lattice parameters and volume took place because of the interaction of KCdCl3 with rGO and C60. A minor deviation is observed

in calculated results compared to standard values, showing the phase purity of the prepared samples. The crystallite size increases, and dislocation density decreases. It may be due to the agglomeration of rGO and C60.

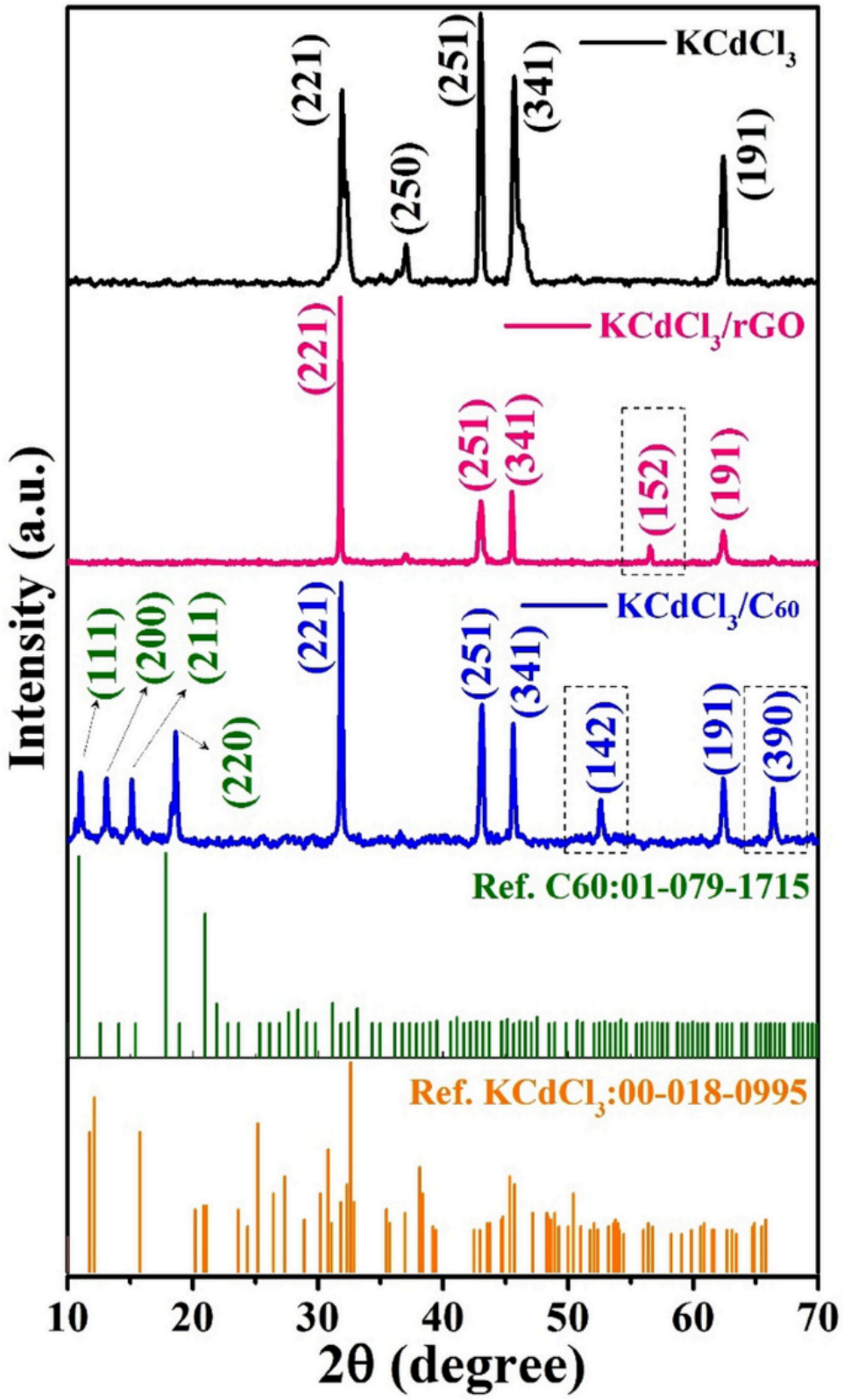

Fig. 1 XRD diffraction pattern of KCdCl3, KCdCl3/rGO, KCdCl3/C60 nanostructures along with standard fullerene-C60 and KCdCl3 perovskite

Table 1 Structural parameters of all compositions

Samples	a (Å)	b (Å)	c (Å)	Volume ($Å^3$)	d-spacing	Crystallite size (nm)	Lattice strain $\varepsilon \times 10^{-3}$	Dislocation density $\delta \times 10^{-4}$ (nm^{-2})
$KCdCl_3$	8.603	14.594	4.243	532.706	1.896	42	0.915	5.596
$KCdCl_3$/rGO	8.985	14.639	4.009	527.302	2.003	84	0.708	1.404
$KCdCl_3$/C60	8.782	14.532	4.090	521.961	1.920	57	0.648	3.131

3.2 Scanning electron microscopy (SEM) and energy-dispersive X-ray (EDX) analysis

Morphological properties of KCdCl3, KCdCl3/rGO, and KCdCl3/C60 nanocomposites were analyzed by SEM at different magnifications, as shown in Fig. 2a–c. From the SEM images of pure KCdCl3 (Fig. 2a–a4) observed irregular shape formation of aggregated particles and granular-like morphology, which can be differentiated at different magnifications. The obtained morphology exhibited a porous-like structure which is beneficial in the storage mechanism. In comparison to pure KCdCl3, in KCdCl3/rGO and KCdCl3/C60 nanocomposite, the nanoparticles of KCdCl3 adhered over rGO and C60 sheet as depicted in Fig. 2b–b4, c–c4, which provide the rapid and smooth pathway for the ions/charge transportation and inhibit the structural collapse during charging–discharging [28, 29]. Additionally, elemental acquiesce, and compositions of prepared samples were carried out by EDX, confirming the presence of K, Cd, Cl, and C depicted in Fig. 3, and the formation of KCdCl3/rGO and KCdCl3/C60 nanocomposites. The atomic and weight% (%) of elements are listed in Table 2.

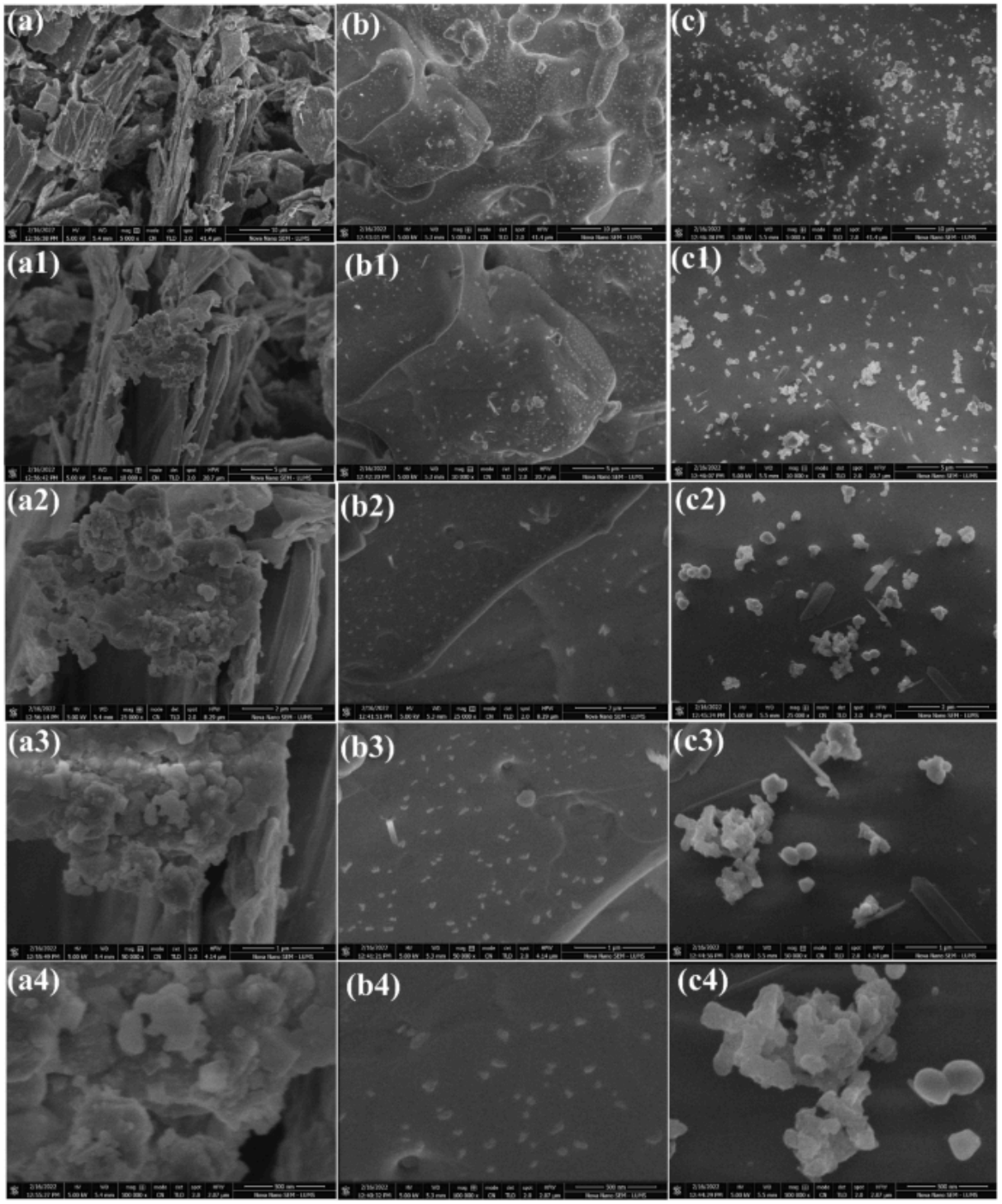

Fig. 2 SEM images of a–a4 KCdCl3, b–b4 KCdCl3/rGO, and c–c4 KCdCl3/C60 nanostructures

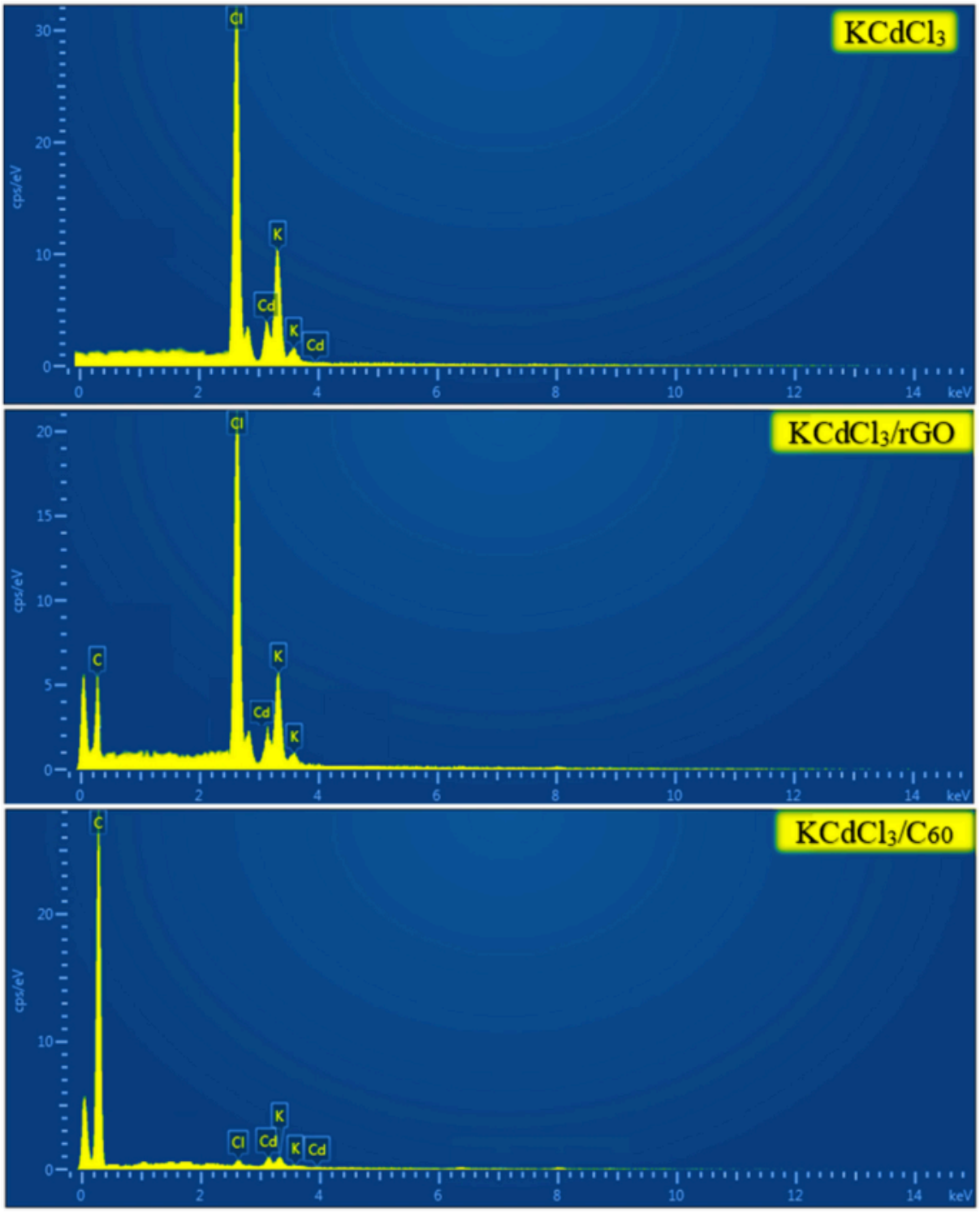

Fig. 3 EDX spectra of a KCdCl3, b KCdCl3/rGO, and c KCdCl3/C60 nanostructures

Elements	$KCdCl_3$		$KCdCl_3$/rGO		$KCdCl_3$/C60	
	Weight%	Atomic%	Weight%	Atomic%	Weight%	Atomic%
K	14.43	18.36	13.32	10.67	12.35	9.66

Cd	40.00	17.70	33.00	9.19	32.00	8.70
Cl	45.57	63.94	34.68	30.62	35.65	30.74
C	–	–	19.00	49.52	20.00	50.90
Total	100	100	100	100	100	100

Table 2 Elemental composition from EDX for all compositions

3.3 Brunauer–Emmett–Teller (BET)

BET analysis was performed to evaluate the surface area, pore size distribution, and pore volume. The porosity, volume, and specific surface area of the pure KCdCl3, KCdCl3/rGO, and KCdCl3/C60 are depicted in Fig. 4. Nanocomposites were evaluated by N2 adsorption/desorption measurements and are listed in Table 3. The detailed BET analysis parameters and related graphs are provided in supporting information. The adsorption isotherms show type III with an H3 type of hysteresis loop, as depicted in Fig. 4a–c. Using Barrett Joyner Halenda (BJH), the pore volume distribution curves of pure KCdCl3, KCdCl3/rGO, and KCdCl3/C60 are depicted in Fig. 4. Nanocomposites are drawn, as shown in Fig. S1, and surface area distributions are presented in Fig. 4d–f. The pore sizes of pure KCdCl3, KCdCl3/rGO, and KCdCl3/C60 nanocomposites are 47.2705 Å, 111.5508 Å, and 459.4871Å, respectively. The results show that pore size, surface area, and pore volume are larger in the case of KCdCl3/C60 nanocomposite than in others. The increment in the surface area can increase the number of electroactive sites for charge accumulation (certainly essential for energy storage application), which enhance the specific capacitance [30, 31]. Furthermore, the porosity increases in KCdCl3/C60 nanocomposite because of the heterostructure of KCdCl3 with C60 confirmed from SEM images. These results are favorable for the energy storage mechanism.

Compositions	**Surface area (m^2/g)**	**Pore volume (cm^3/g)**	**Pore size (Å)**
$KCdCl_3$	3.6052	0.004261	47.2705
$KCdCl_3$/rGO	6.0488	0.016869	111.5508
$KCdCl_3$/C60	11.4688	0.131744	459.4871

Table 3 Surface area, pore volume, and pore size of grown samples obtained from BET analysis

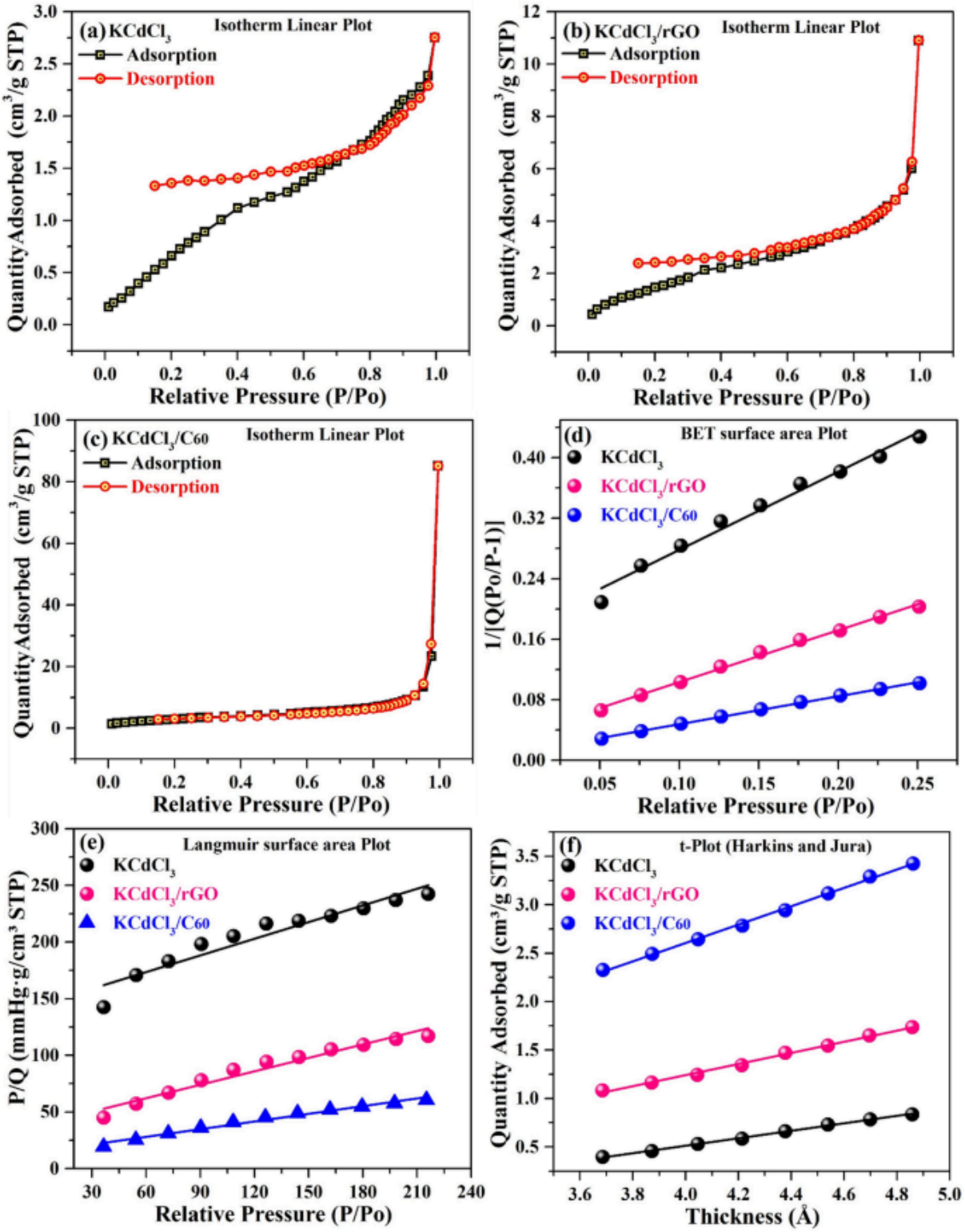

Fig. 4 a–c BET N2 adsorption–desorption curves, d Bet surface area plot, e Langmuir surface area plot, and f) t-plot for KCdCl3, KCdCl3/rGO, and KCdCl3/C60 nanostructures

3.4 Current–voltage (I–V) measurements

The I–V curve of the as-synthesized nanocomposite at a voltage from − 10 to 10 V is measured at room temperature and is shown in Fig. 5a. The results indicate that the

KCdCl3/C60 nanocomposite has a greater current value at end voltage values than others. The IV curve also displays that the synthesized samples have ohmic nature. The electrical conductivity (σ) and electrical resistivity (ρ) were calculated using the equation [32] and are shown in Fig. 5b. The existence of the rGO and C60 in the nanocomposite causes an increase in conductivity, revealing that the formation of the nanocomposite can enhance the conductivity of KCdCl3. As the ability of energy storage is related to contact resistance, prepared samples are efficient materials for energy storage devices.

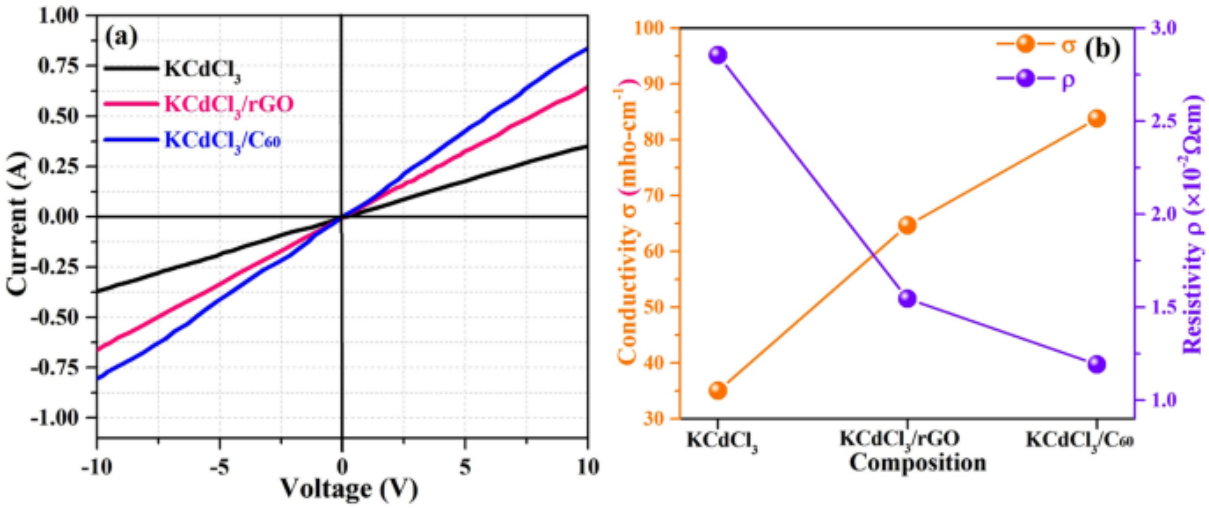

Fig. 5 a IV curve and b electrical conductivity and resistivity values, for KCdCl3, KCdCl3/rGO, and KCdCl3/C60 nanostructures

3.5 Electrochemical activity

In order to evaluate the performance of pure KCdCl3, KCdCl3/rGO, and KCdCl3/C60 nanocomposites, different electrochemical characterizations, including CV, GCD, LSV, EIS, and ECSA, were performed in 1 M KOH electrolyte solution.

3.5.1 Cyclic voltammetry (CV)

CV test is an efficient electrochemical technique used to check the capacitive behavior at different scan rates of the synthesized material [33]. The CV loops of the pure KCdCl3, KCdCl3/rGO, and KCdCl3/C60 nanocomposite electrodes at different scan rates 5, 10, 15, 20, 25, 30 mV/s are taking operating potential between − 0.05 and 0.5 V as shown in Fig. 6a–c. All the CV cycles show paired redox peaks with quasi-rectangular shapes, which confirms the pseudocapacitive nature of all prepared electrodes. Redox (oxidation–reduction) peaks shifted toward higher potential by increasing the scan rate, showing an increment in ion-diffusion resistance. Also, the shape uniformity of CV curves at various sweep rates proved the higher reversibility of redox reaction. The Csp of all the synthesized electrodes at different scan rates was computed by using the given equation [34]:

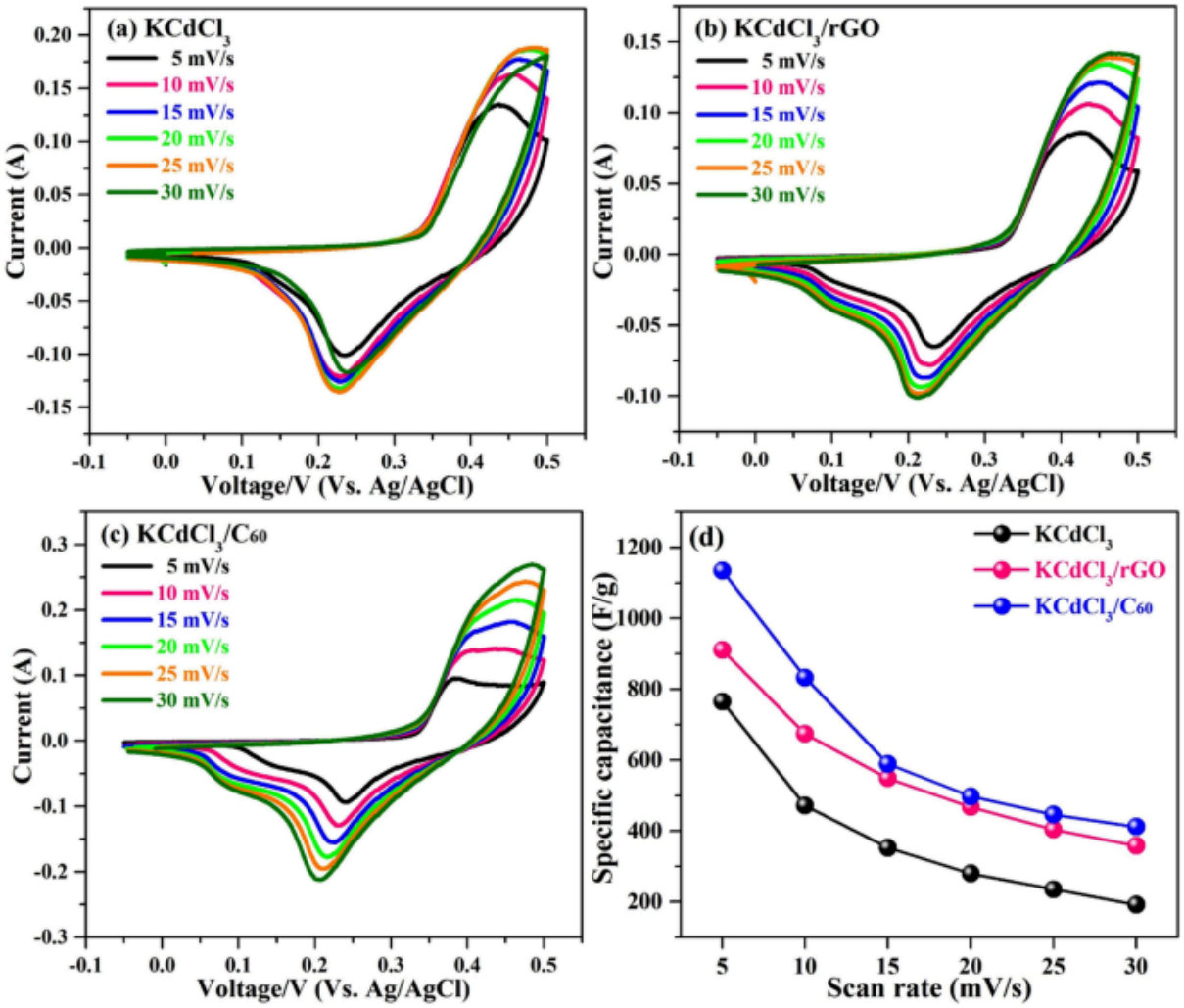

Fig. 6 CV loops a KCdCl3, b KCdCl3/rGO, c KCdCl3/C60 nanostructures at varying scan rates, and d specific capacitance values at various sweep rate

$$Csp=\int I/smVdV \qquad (1)$$

Here, $\int IdV$ gives the area of CV curves, 'V' is the operating potential, 's' is the sweep rate, and 'm' is the electrode's loaded mass. The specific capacitance value of pure KCdCl3, KCdCl3/rGO, and KCdCl3/C60 nanocomposites and calculated values are 765 F/g, 911 F/g, and 1135 F/g, respectively. It is observed that KCdCl3/C60 nanocomposite shows a high capacitance value as compared to others due to the mesoporous nature of C60, which provides an easy pathway to transfer the electrolyte ions in the electrode surface. The specific capacitance (Csp) versus different scan rates is manifested in Fig. 6d. At a high scan rate, specific capacitance decreases due to polarization influence, and there is a short time to diffuse the electrolyte ions on the electrode surface, resulting in a decrement in storage capability. Contrarily, at a low sweep rate, maximum active sites are available for the participation to store charge, leading to higher specific capacitance. The comparison of the specific capacitance of the fabricated electrode and other reported work is listed in Table 4.

S. no.	Material	Method of preparation	Electrolyte	*Csp*	Scan rate	References
1.	$CsPbBr_3$	Chemical	1 M KOH	121 F/g	5mV/s	[14]
2.	$MAPbI_3$	Spin coating	2 M H_3PO_4	402 F/g	10 mV/s	[43]
3.	$MA_3Bi_2I_9$	Spin coating	2 M H_3PO_4	550 F/g	10 mV/s	[43]
4.	$CH_3NH_3PbBr_3$	Spin coating	TBATFB/CH_2Cl_2	54.36 F/g	5 mV/s	[12]
5.	$CH_3NH_3PbBr_3$	Inverse temperature crystallization	DMF	36.82 F/g	5mV/s	[44]
6.	$MAPbI_3$@NiO	Wet chemical	1 g/mL H_3PO_4	407 F/g	10 mV/s	[45]
7	$LaAlO_3$/rGO	hydrothermal		721 F/g	2 mV/s	[42]
8.	$CsPbI_3$	Chemical	Butanol	7.23 mF/cm^2	2 mV/s	[17]
9.	$CH_3NH_3PbI_3$	Chemical	HCl	432 mF/cm^2	5 mA/cm^2	[16]
10.	$CsPbBr_{2.9}I_{0.1}$	Chemical	1 M $LiClO_4$	150 mF/cm^2	0.1 mA/cm^2	[13]
11	$LaFeO_3$/rGO	In-Situ microwave irradiation	1 M Na_2SO_4	170 F/g	10 mV/s	[46]
12	$(CN_2SH_5)_3BiI_6$	Solution	$NaClO_4$	1030 F/g	10 mV/s	[47]
13	$LaMnO_{3+\delta}$	Reverse phase hydrolysis	1 M KOH	586.7 F/g	2 mV/s	[48]
14	$LaMnO_3$/rGO/PANI	Situ polymerization	KOH	802 F/g	2 mV/s	[49]
15	$LaNiO_3$	Sol–gel	3 M LiOH	106.58 F/g	5 mV/s	[50]
16	$SrMnO_3$	Sol–gel assisted electrospinning	0.5 M Na_2SO_4	446.8 F/g	10 mV/s	[51]

17	$KCdCl_3$/rGO	Solvothermal	1 M KOH	911	5 mV/s	This work
18	$KCdCl_3$/C60	Solvothermal	1 M KOH	1135	5 mV/s	This work

Table 4 Comparison of specific capacitance from CV of grown electrode material with other reported materials

3.5.2 Cycling stability

To examine the electrochemical stability of highly efficient KCdCl3/rGO and KCdCl3/C60 electrodes, CV cycles were conducted for 3000th cycles at 5 mV/s scan rate with potential window − 0.05 to 0.5 V in KOH alkaline solution. Figure 7a exhibits the cyclic retention (%) of both electrodes, which shows that the capacitance ability remained unchanged, evident in the favorable reversibility and good electrochemical stability of fabricated KCdCl3/rGO and KCdCl3/C60 electrodes. Furthermore, it is observed that the KCdCl3/rGO electrode retained 97% of the original capacitance, while the KCdCl3/C60 electrode retained 97.6% of the original capacitance. Finally, it is concluded that KCdCl3/C60 electrode shows high specific capacitance with high durability and outstanding cyclic stability.

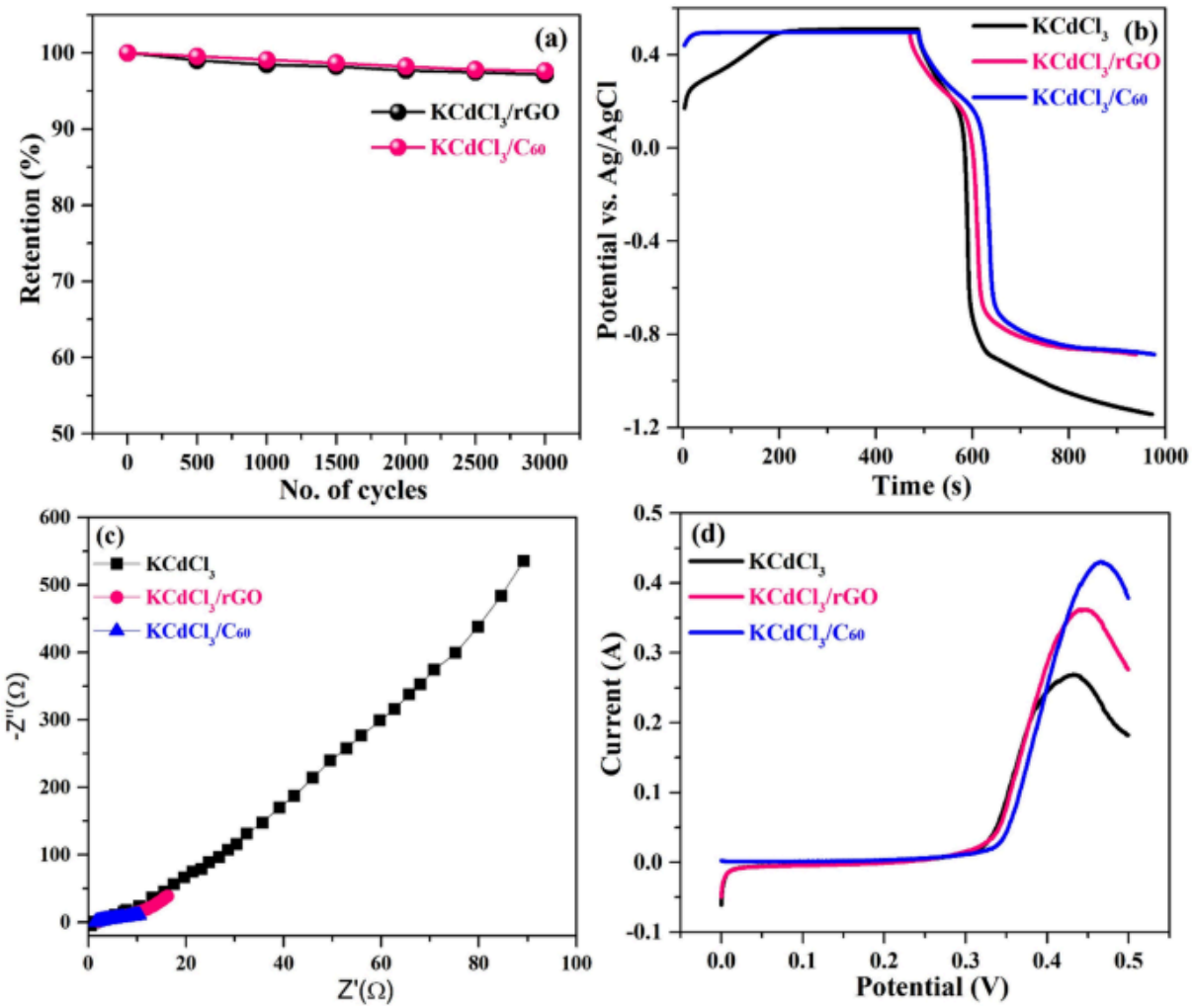

Fig. 7 a capacitive retention (%) for KCdCl3/rGO and KCdCl3/C60 electrodes, b GCD profile, c Nyquist plots, and d LSV curves, for all compositions

3.5.3 Galvanostatic charge–discharge (GCD)

To further ensure the electrochemical performance of all prepared electrodes, the GCD test was conducted at a constant current density of 1 A/g with operating potential (− 1.2 to 0.5 V), as illustrated in Fig. 7b. Figure 7b shows GCD curves of the fabricated pure KCdCl3, KCdCl3/rGO, and KCdCl3/C60 electrodes depicting the non-linear triangular shape, which manifested the pseudocapacitive nature of all electrodes. To measure the specific capacitance (Csp), energy density (E), and power density (P) from the GCD curve, the following relations were used [35].

$$Csp=(Id\times Td)/(\Delta V\times m) \quad (2)$$

$$E=0.5\times Csp\times \Delta V\text{^}2/3.6 \quad (3)$$

$$Ps=E\times 3600/Td \quad (4)$$

ΔV is the operating potential, Id is the discharge current, Td is the discharge time, and ΔV^2 represents the voltage range. The calculated specific capacitance (Csp) was 570, 775, 1420

F/g with energy density 824, 1120, 2052 Wh/Kg and power density 4.58, 4.99, 4.19 W/Kg at a current density of 1 A/g for pure KCdCl3, KCdCl3/rGO, and KCdCl3/C60 electrodes, respectively. Furthermore, we observed that the maximum value of the specific capacitance of the KCdCl3/C60 electrode is assigned to the longer discharging time than other fabricated electrodes. Considering the above finding, it is concluded that the electrode (KCdCl3/C60) possesses outstanding capacitive performance compared to the other. The specific capacitance from GCD of synthesized electrode and data collected from the literature is listed in Table 5.

S. no.	Material	Method of preparation	Electrolyte	*Csp*	Current density	References
1	$CsPbBr_3$	Chemical	1 M KOH	116 F/g	1.0 A/g	[14]
2	$CH_3NH_3PbBr_3$	Spin coating	TBATFB/CH_2Cl_2	40.8 F/g	0.3 A/g	[52]
3	$LaFeO_3$/rGO	Hydrothermal	2 M KOH	367.4 F/g	1 A/g	[53]
4	$(CN_2SH_5)_3BiI_6$	Solution	$NaClO_4$	899 F/g	0.22 A/g	[47]
5	PANI	Interfacial polymerization	1 M HClO4	554 F/g	10 mA/g	[54]
6	GO/PANI	Soft chemical rout	1 M H_2SO_4	531 F/g	0.2 A/g	[55]
7	$LaNiO_3$	Template free method	6 M KOH	422 F/g	1.0 A/g	[56]
8	$LaNiO_3$	Wet chemical	3 M LiOH	106.58 F/g	1 A/g	[50]
9	$LaCoO_3$/rGO	Solvothermal approach	–	317 F/g	1.75 A/g	[57]
10	La_2CuMnO_6	Hydrothermal	2 M KOH	205.5 F/g	0.25 A/g	[58]
11	rGO/PANI	In situ polymerization	–	1045 F/g	0.1 A/g	[59]
12	$La_{1-x}Sr_xMnO_3$	Sol–gel	1 MKOH	102 F/g	1.0 A/g	[60]
13	$KCdCl_3$/rGO	Solvothermal	1 M KOH	775	1.0 A/g	This work

14	$KCdCl_3$/C60	Solvothermal	1 M KOH	1420	1.0 A/g	This work

Table 5 Comparison of specific capacitance from GCD of grown electrode material with other reported materials

3.5.4 Electrochemical impedance spectroscopy (EIS)

EIS is often used to study the fabricated electrode's charge transfer kinetics, ions diffusion rate, and capacitance [36]. Figure 7c shows the combined pattern of all electrodes, which clearly shows that KCdCl3/C60 has a small semi-circular pattern with very small polarization resistance and charge transfer resistance that fast transportation of ions at the electrode interface that gives high Cs and shows pseudocapacitive nature [37]. From the results, we concluded that KCdCl3/C60 electrode provides more active sites to make extra conductive electrode material.

3.5.5 Linear sweep voltammetry (LSV)

LSV was used to obtain the intrinsic catalytic efficiency and maximum current response of KCdCl3, KCdCl3/rGO, and KCdCl3/C60 electrodes interacting with electrolytes. Figure 7d presents the potential dynamic LSV curves of the above-synthesized electrodes. LSV curves were taken out between the potential windows of 0 and 0.5 V, conducted in 1.0 M KOH solution. Maximum response in current density with increasing scan rates indicates the electrodes' large integrated peak area. The higher current density of the KCdCl3/C60 electrode (Fig. 7d) has a much higher peak than the KCdCl3 and KCdCl3/rGO electrodes, respectively, that happens due to the high electrochemical surface area (58.6 cm^2), large pore size (= 459.4871 Å) ,and morphological/structural effects as well.

3.5.6 Electrochemical active surface area (ECSA)

Besides the LSV, ECSA is another main parameter used to calculate the active surface area of the electrode. To investigate the electrochemical performance of the KCdCl3, KCdCl3/rGO, and KCdCl3/C60 fabricated electrodes, a non-faradic region is assumed under CV curves within potential window − 2.5 to 0.5 V. CV cycles under the narrow potential window were recorded at varying scan rates, i.e., 10, 20, 30, and 40 mV/s shown in Fig. 8a–c. Then, electrochemical double-layer capacitance (Cdl) was measured using these curves. After that, the calculated active surface area and the measured Cdl was divided by the capacitance value (0.040 mF/cm^2) for the flat electrode, which is generally within the range of 0.01–0.05 mF/cm [38]. Moreover, ECSA can be determined using the given relation [39]:

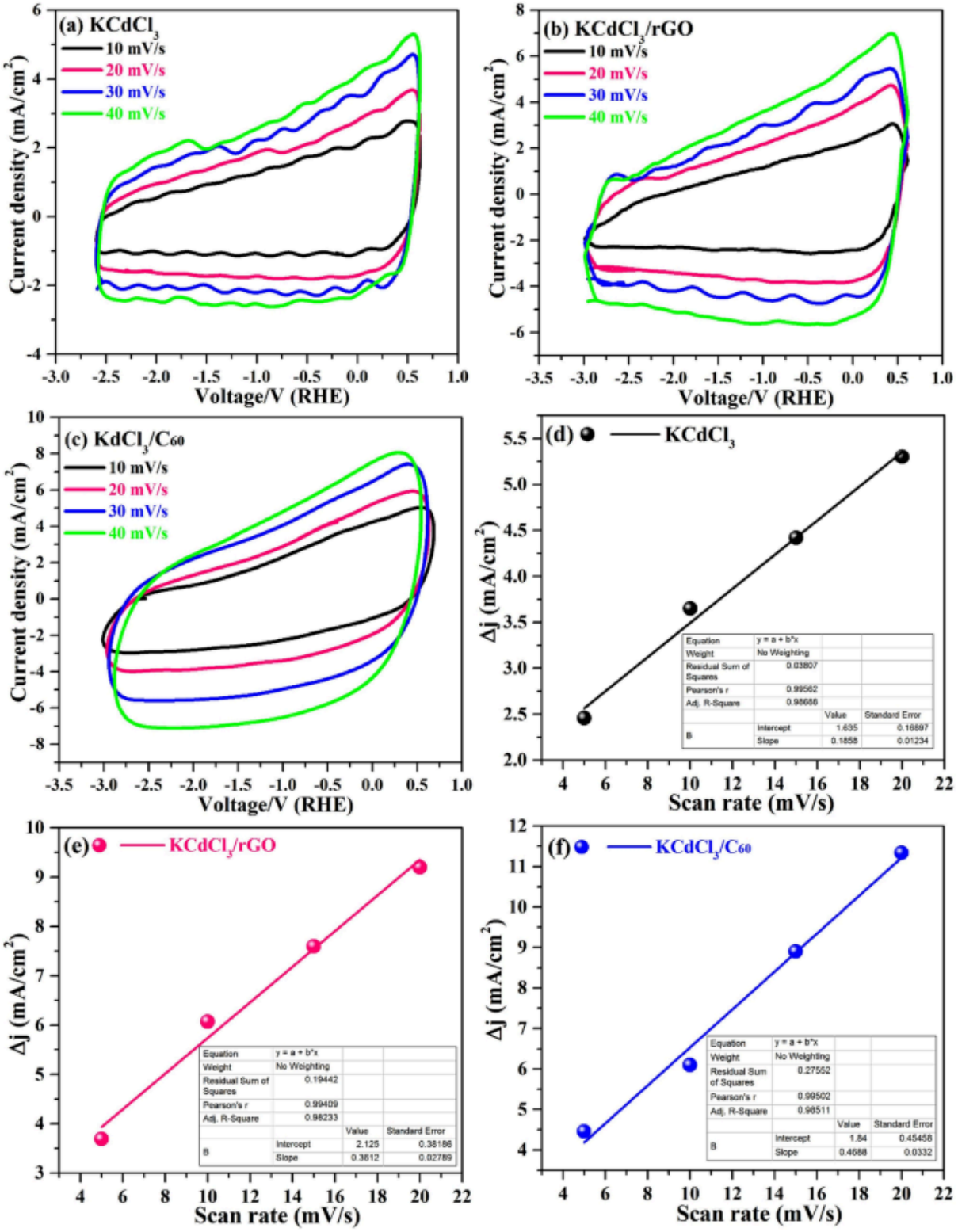

Fig. 8 ECSA loops a KCdCl3, b KCdCl3/rGO, c KCdCl3/C60 nanostructures at varying scan rates, and d–f linear fitting plots for calculating Cdl and ECSA.

$$ECSA = Cdl / Cs \qquad (5)$$

The double-layer capacitance (Cdl) and ECSA values of KCdCl3, KCdCl3/rGO, and KCdCl3/C60 electrodes were 0.0929, 0.1806, and 0.2344 μF and 23.225, 45.15, and 58.60

cm^2, respectively. From the results, we concluded that the ECSA value of the KCdCl3/C60 electrode is in good agreement with the BET surface area.

3.5.6.1 Performance evaluation

The exceptional electrochemical performance and stability of KCdCl3/C60 electrode is compared to other electrodes due to fullerene-C60, which has a unique π-electron conjugated system and has hierarchical pore structure and active redox sites, and possess high electrical conductivity [40, 41]. Moreover, the halide perovskite materials contain low activation energy. Also, the electronic traps and ion kinetics significantly enhance the mobility of the ions for interstitials [42]. Furthermore, the incorporation of fullerene (C60) in KCdCl3 causes to increase in the porosity, which improves the capacitive performance. The outstanding performance is attributed to high porosity and distinctive morphology, as confirmed by BET analysis, which easily exhibits transportation of ions/charges, leading to decreased charge transfer and solution resistance.

4 Conclusion

This article comprehensively described the structural and electrochemical properties of the halide perovskite KCdCl3 and their composite with rGO (KCdCl3/rGO) and C60 (KCdCl3/C60) successfully fabricated by the solvothermal route. An orthorhombic phase of KCdCl3 was confirmed from XRD spectra, and EDX confirms the existence of K, Cd, Cl, and C. BET result provided the high surface area, pore radius, and pore volume of C60-based electrode. The electrochemical analysis provided that the electrode KCdCl3/C60 delivered high specific capacitance 1135 at 5 mV/s and attained retention 97.6% after 3000th cycles, which signifies good stability. Finally, we conclude that KCdCl3/C60-based electrode provides more active sites for electrochemical response and concise the pathway for charge/ions movement, are highly suitable and competent for next-generation supercapacitor electrode material.

References

1. Raheem A, Abbasi SA, Memon A et al (2016) Renewable energy deployment to combat energy crisis in Pakistan. Energy Sustain Soc 6:16. https://doi.org/10.1186/s13705-016-0082-z

2. Yao L, Yang B, Cui H et al (2016) Challenges and progresses of energy storage technology and its application in power systems. J Mod Power Syst Clean Energy 4:519–528. https://doi.org/10.1007/s40565-016-0248-x

3. Gür TM (2018) Review of electrical energy storage technologies, materials and systems: challenges and prospects for large-scale grid storage. Energy Environ Sci 11:2696–2767. https://doi.org/10.1039/C8EE01419A

4. Shaqsi AZ, Sopian K, Al-Hinai A (2020) Review of energy storage services, applications, limitations, and benefits. Energy Rep 6:288–306. https://doi.org/10.1016/j.egyr.2020.07.028

5. Kebede AA, Kalogiannis T, Van Mierlo J, Berecibar M (2022) A comprehensive review of stationary energy storage devices for large scale renewable energy sources grid integration. Renew Sustain Energy Rev 159:112213. https://doi.org/10.1016/j.rser.2022.112213

6. Jalal NI, Ibrahim RI, Oudah MK (2021) A review on supercapacitors: types and components. J Phys Conf Ser 1973:12015. https://doi.org/10.1088/1742-6596/1973/1/012015

7. Nagarajarao SH, Nandagudi A, Viswanatha R et al (2022) Recent Developments in supercapacitor electrodes: a mini review. ChemEngineering 6:5

8. Najib S, Erdem E (2019) Current progress achieved in novel materials for supercapacitor electrodes: mini review. Nanoscale Adv 1:2817–2827. https://doi.org/10.1039/C9NA00345B

9. Popoola I, Gondal M, Oloore L et al (2020) Fabrication of organometallic halide perovskite electrochemical supercapacitors utilizing quasi-solid-state electrolytes for energy storage devices. Electrochim Acta 332:135536. https://doi.org/10.1016/j.electacta.2019.135536

10. Pious JK, Lekshmi ML, Muthu C et al (2017) Zero-dimensional methylammonium bismuth iodide-based lead-free perovskite capacitor. ACS Omega 2:5798–5802. https://doi.org/10.1021/acsomega.7b00973

11. Chen T-W, Ramachandran R, Chen S-M et al (2020) Developing low-cost, high performance, robust and sustainable perovskite electrocatalytic materials in the electrochemical sensors and energy sectors: “an overview.” Catalysts. 10:938

12. Kumar R, Shukla PS, Varma GD, Bag M (2021) Synthesis of porous electrode from CH3NH3PbBr3 single crystal for efficient supercapacitor application: role of morphology on the charge storage and stability. Electrochim Acta 398:1–26. https://doi.org/10.1016/j.electacta.2021.139344

13. Ng CH, Lim HN, Hayase S et al (2018) Cesium lead halide inorganic-based perovskite-sensitized solar cell for photo-supercapacitor application under high humidity condition. ACS Appl Energy Mater 1:692–699. https://doi.org/10.1021/acsaem.7b00103

14. Thakur S, Paul T, Maiti S, Chattopadhyay KK (2021) All-inorganic CsPbBr3 perovskite as potential electrode material for symmetric supercapacitor. Solid State Sci 122:106769. https://doi.org/10.1016/j.solidstatesciences.2021.106769

15. Kostopoulou A, Brintakis K, Nasikas NK, Stratakis E (2019) Perovskite nanocrystals for energy conversion and storage. Nanophotonics 8:1607–1640. https://doi.org/10.1515/nanoph-2019-0119

16. Slonopas A, Ryan H, Norris P (2019) Ultrahigh energy density CH3NH3PbI3 perovskite based supercapacitor with fast discharge. Electrochim Acta 307:334–340. https://doi.org/10.1016/j.electacta.2019.03.221

17. Maji P, Ray A, Sadhukhan P et al (2018) Fabrication of symmetric supercapacitor using cesium lead iodide (CsPbI3) microwire. Mater Lett 227:268–271. https://doi.org/10.1016/j.matlet.2018.05.101

18. Malik MTU, Sarker A, Mahmud Rahat SMS, Shuchi SB (2021) Performance enhancement of graphene/GO/rGO based supercapacitors: a comparative review. Mater Today Commun 28:102685. https://doi.org/10.1016/j.mtcomm.2021.102685

19. Cai Z, Ma YF, Wang M et al (2022) Engineering of electrolyte ion channels in MXene/holey graphene electrodes for superior supercapacitive performances. Rare Met 41:2084–2093. https://doi.org/10.1007/s12598-021-01935-6

20. Zhou M, Yan SX, Wang Q et al (2022) Walnut septum-derived hierarchical porous carbon for ultra-high-performance supercapacitors. Rare Met 41:2280–2291. https://doi.org/10.1007/s12598-021-01957-0

21. Ke Q, Wang J (2016) Graphene-based materials for supercapacitor electrodes—a review. J Mater 2:37–54. https://doi.org/10.1016/j.jmat.2016.01.001

22. Ramadan A, Anas M, Ebrahim S et al (2020) Polyaniline/fullerene derivative nanocomposite for highly efficient supercapacitor electrode. Int J Hydrogen Energy 45:16254–16265. https://doi.org/10.1016/j.ijhydene.2020.04.093

23. Ali SR, Faisal MM, Sanal KC, Iqbal MW (2021) Impact of carbon-based charge transporting layer on the performance of perovskite solar cells. Sol Energy 221:254–274. https://doi.org/10.1016/j.solener.2021.04.040

24. Bairi P, Maji S, Hill JP et al (2019) Mesoporous carbon cubes derived from fullerene crystals as a high rate performance electrode material for supercapacitors. J Mater Chem A 7:12654–12660. https://doi.org/10.1039/C9TA00520J

25. Tienne LGP, Candido L, da Cruz S, de SM B et al (2022) Reduced graphene oxide synthesized by a new modified Hummer's method for enhancing thermal and crystallinity properties of poly(vinylidene fluoride). J Mater Res Technol 18:4871–4893. https://doi.org/10.1016/j.jmrt.2022.04.092

26. Marcano DC, Kosynkin DV, Berlin JM et al (2010) Improved synthesis of graphene oxide. ACS Nano 4:4806–4814. https://doi.org/10.1021/nn1006368

27. Nazim M, Kim JH (2020) Controlled size growth of thermally stable organometallic halide perovskite microrods: synergistic effect of dual-doping, lattice strain engineering, antisolvent crystallization, and band gap tuning properties. ACS Omega 5:16106–16119. https://doi.org/10.1021/acsomega.0c01667

28. Ahmad K, Mohammad A, Mathur P, Mobin SM (2016) Preparation of SrTiO3 perovskite decorated rGO and electrochemical detection of nitroaromatics. Electrochim Acta 215:435–446. https://doi.org/10.1016/j.electacta.2016.08.123

29. Jing F, Ma Z, Wang J et al (2022) Oxygen vacancy inducing phase transition during charge storage in MnOx@rGO supercapacitor electrode. Chem Eng J 435:135103. https://doi.org/10.1016/j.cej.2022.135103

30. Amar VS, Houck JD, Maddipudi B et al (2021) Hydrothermal liquefaction (HTL) processing of unhydrolyzed solids (UHS) for hydrochar and its use for asymmetric supercapacitors with mixed (Mn,Ti)-Perovskite oxides. Renew Energy 173:329–341. https://doi.org/10.1016/j.renene.2021.03.126

31. Ajay KM, Dinesh MN, Byatarayappa G et al (2021) Electrochemical investigations on low cost KOH activated carbon derived from orange-peel and polyaniline for hybrid supercapacitors. Inorg Chem Commun 127:108523. https://doi.org/10.1016/j.inoche.2021.108523

32. Munawar T, Rehman MN, ur, Nadeem MS et al (2021) Facile synthesis of Cr-Co co-doped CdO nanowires for photocatalytic, antimicrobial, and supercapacitor applications. J Alloys Compd 885:160885. https://doi.org/10.1016/j.jallcom.2021.160885

33. Karthikeyan S, Narenthiran B, Sivanantham A et al (2021) Supercapacitor: Evolution and review. Mater Today Proc. https://doi.org/10.1016/j.matpr.2021.02.526

34. Pallavolu MR, Gaddam N, Banerjee AN et al (2022) Facile construction and controllable design of CoTiO3@Co3O4/NCNO hybrid heterojunction nanocomposite electrode for high-performance supercapacitors. Electrochim Acta 407:139868. https://doi.org/10.1016/j.electacta.2022.139868

35. Yang D, Xu M, Liang X et al (2022) Facile synthesis of Pr-doped Co3O4 nanoflakes on the nickel-foam for high performance supercapacitors. Electrochim Acta 406:139815. https://doi.org/10.1016/j.electacta.2021.139815

36. Ates M (2011) Review study of electrochemical impedance spectroscopy and equivalent electrical circuits of conducting polymers on carbon surfaces. Prog Org Coat 71:1–10. https://doi.org/10.1016/j.porgcoat.2010.12.011

37. Xavier AR, Ravichandran AT, Vijayakumar S et al (2022) Synthesis and characterization of Sr-doped CdO nanoplatelets for supercapacitor applications. J Mater Sci Mater Electron 33:8426–8434. https://doi.org/10.1007/s10854-021-06329-z

38. Sehrish R, Manzoor S, Munawar T et al (2022) Hydrothermal preparation of LaNdZr2O7–SnSe nanocomposite for electrochemical supercapacitor and degradation of contaminants' applications. J Energy Storage 52:104930. https://doi.org/10.1016/j.est.2022.104930

39. Munawar T, Mukhtar F, Nadeem MS et al (2022) Fabrication of dual Z-scheme TiO2-WO3-CeO2 heterostructured nanocomposite with enhanced photocatalysis, antibacterial, and electrochemical performance. J Alloys Compd 898:162779. https://doi.org/10.1016/j.jallcom.2021.162779

40. Puente Santiago AR, Fernandez-Delgado O, Gomez A et al (2021) Fullerenes as Key components for low-dimensional (photo)electrocatalytic nanohybrid materials. Angew Chem Int Ed 60:122–141. https://doi.org/10.1002/anie.202009449

41. Xu T, Shen W, Huang W, Lu X (2020) Fullerene micro/nanostructures: controlled synthesis and energy applications. Mater Today Nano. https://doi.org/10.1016/j.mtnano.2020.100081

42. Narayanan S, Parikh N, Tavakoli MM et al (2021) Metal halide perovskites for energy storage applications. Eur J Inorg Chem 2021:1201–1212. https://doi.org/10.1002/ejic.202100015

43. Oloore LE, Gondal MA, Popoola IK, Popoola AJ (2020) Cadmium sulfide quantum dots–organometallic halide perovskite bilayer electrode structures for supercapacitor applications. ChemElectroChem 7:486–492. https://doi.org/10.1002/celc.201901969

44. Kumar R, Bag M (2021) Quantifying capacitive and diffusion-controlled charge storage from 3D bulk to 2D layered Halide Perovskite-Based porous electrodes for efficient Supercapacitor applications. J Phys Chem C 125:16946–16954. https://doi.org/10.1021/acs.jpcc.1c05493

45. Oloore LE, Gondal MA, Popoola AJ, Popoola IK (2020) Pseudocapacitive contributions to enhanced electrochemical energy storage in hybrid perovskite-nickel oxide nanoparticles composites electrodes. Electrochim Acta 361:137082. https://doi.org/10.1016/j.electacta.2020.137082

46. Jadhav SB, Malavekar DB, Bulakhe RN et al (2021) Dual-functional electrodeposited vertically grown Ag-La2O3 nanoflakes for non-enzymatic glucose sensing and Energy Storage Application. Surf Interfaces. https://doi.org/10.1016/j.surfin.2021.101018

47. Li T, Mallows J, Adams K et al (2019) Thiourea bismuth iodide: crystal structure, characterization and high performance as an electrode material for supercapacitors. Batter Supercaps 2:568–575. https://doi.org/10.1002/batt.201900005

48. Mefford JT, Hardin WG, Dai S et al (2014) Anion charge storage through oxygen intercalation in LaMnO3 perovskite pseudocapacitor electrodes. Nat Mater 13:726–732. https://doi.org/10.1038/nmat4000

49. Yadav AA, Lokhande AC, Pujari RB et al (2016) The synthesis of multifunctional porous honey comb-like La2O3 thin film for supercapacitor and gas sensor applications. J Colloid Interface Sci 484:51–59. https://doi.org/10.1016/j.jcis.2016.08.056

50. Arjun N, Pan GT, Yang TCK (2017) The exploration of Lanthanum based perovskites and their complementary electrolytes for the supercapacitor applications. Results Phys 7:920–926. https://doi.org/10.1016/j.rinp.2017.02.013

51. Rezanezhad A, Rezaie E, Ghadimi LS et al (2020) Outstanding supercapacitor performance of Nd–Mn co-doped perovskite LaFeO3@nitrogen-doped graphene oxide nanocomposites. Electrochimica Acta 335:135699

52. Grossman PZ (2015) Energy shocks, crises and the policy process: a review of theory and application. Energy Policy 77:56–69. https://doi.org/10.1016/j.enpol.2014.11.031

53. Li J, Luo W, Wang X et al (2022) Preparation and research of high-performance LaFeO3/RGO supercapacitor. J Solid State Electrochem. https://doi.org/10.1007/s10008-022-05165-3

54. Sivakkumar SR, Kim WJ, Choi JA et al (2007) Electrochemical performance of polyaniline nanofibres and polyaniline/multi-walled carbon nanotube composite as an electrode material for aqueous redox supercapacitors. J Power Sources 171:1062–1068. https://doi.org/10.1016/j.jpowsour.2007.05.103

55. Dywili NR, Ntziouni A, Ikpo C et al (2019) Graphene oxide decorated nanometal-poly(anilino-dodecylbenzene sulfonic acid) for application in high performance supercapacitors. Micromachines 10:1–17. https://doi.org/10.3390/mi10020115

56. Shao T, You H, Zhai Z et al (2017) Hollow spherical LaNiO3 supercapacitor electrode synthesized by a facile template-free method. Mater Lett 201:122–124. https://doi.org/10.1016/j.matlet.2017.04.143

57. Vats AK, Kumar A, Rajput P, Kumar A (2022) Engineered perovskite LaCoO3/rGO nanocomposites for asymmetrical electrochemical supercapacitor application. J Mater Sci Mater Electron 33:2590–2606. https://doi.org/10.1007/s10854-021-07464-3

58. Singh J, Goutam UK, Kumar A (2019) Hydrothermal synthesis and electrochemical performance of nanostructured cobalt free La2CuMnO6. Solid State Sci 95:1–14. https://doi.org/10.1016/j.solidstatesciences.2019.06.016

59. Luo Z, Zhu L, Huang Y, Tang H (2013) Effects of graphene reduction degree on capacitive performances of graphene/PANI composites. Synth Met 175:88–96. https://doi.org/10.1016/j.synthmet.2013.05.008

60. Dong C, Wu G, Wang Z et al (2020) Supercapacitor performance of perovskite La Sr MnO. Dalt Trans. https://doi.org/10.1039/C7DT03134C

Authors and Affiliations

Institute of Physics, The Islamia University of Bahawalpur, Bahawalpur, 63100, Pakistan
Muhammad Riaz, Tauseef Munawar, Muhammad Shahid Nadeem, Faisal Mukhtar & Faisal Iqbal

Nanoscience and Technology Department, National Centre for Physics, QAU Campus, Islamabad, 45320, Pakistan
Syed Danish Ali

Institute of Chemical Sciences, Bahauddin Zakariya University, Multan, 60800, Pakistan
Sumaira Manzoor & Muhammad Naeem Ashiq

Corresponding author

Correspondence to Faisal Iqbal.